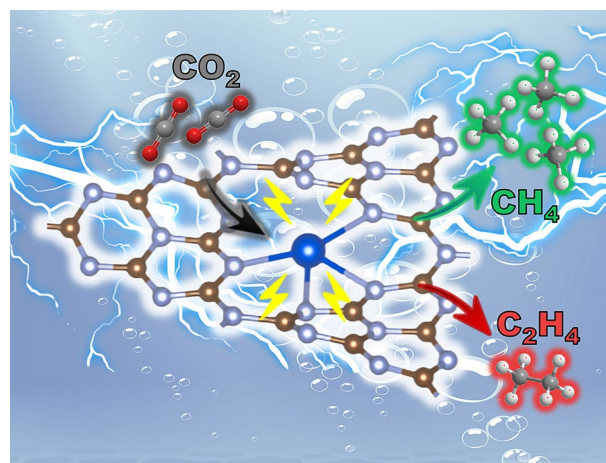# Nano-Micro Letters

ARTICLE

Atomic Cu Sites Engineering Enables Efficient CO_2 Electroreduction to Methane with High CH_4/C_2H_4 Ratio

Minhan Li[1,2], Fangzhou Zhang[1], Min Kuang[1], Yuanyuan Ma[1] ✉, Ting Liao[3], Ziqi Sun[3], Wei Luo[1], Wan Jiang[1], Jianping Yang[1] ✉

HIGHLIGHTS

- The Cu-doped graphitic carbon nitride (g-C_3N_4) material is synthesized by an in situ thermal polymerization strategy, through which the atomic dispersion and coordination structure of Cu on g-C_3N_4 are realized by regulating the doping level of Cu.

- High Faraday efficiency of CH_4 of 49.04% and a maximum CH_4/C_2H_4 ratio up to 35.03 are achieved for the first time on g-C_3N_4-supported Cu single-atom catalyst.

- Structure–activity relationship analysis based on experimental and theoretical studies demonstrates the well-defined Cu single atoms coordinated with N atoms in the nitrogen cavity of g-C_3N_4 are active sites for CO_2-to-CH_4.

ABSTRACT Electrochemical reduction of CO_2 into high-value hydrocarbons and alcohols by using Cu-based catalysts is a promising and attractive technology for CO_2 capture and utilization, resulting from their high catalytic activity and selectivity. The mobility and accessibility of active sites in Cu-based catalysts significantly hinder the development of efficient Cu-based catalysts for CO_2 electrochemical reduction reaction (CO_2RR). Herein, a facile and effective strategy is developed to engineer accessible and structural stable Cu sites by incorporating single atomic Cu into the nitrogen cavities of the host graphitic carbon nitride (g-C_3N_4) as the active sites for CO_2-to-CH_4 conversion in CO_2RR. By regulating the coordination and density of Cu sites in g-C_3N_4, an optimal catalyst corresponding to a one Cu atom in one nitrogen cavity reaches the highest CH_4 Faraday efficiency of 49.04% and produces the products with a high CH_4/C_2H_4 ratio over 9. This work provides the first experimental study on g-C_3N_4-supported single Cu atom catalyst for efficient CH_4 production from CO_2RR and suggests a principle in designing highly stable and selective high-efficiency Cu-based catalysts for CO_2RR by engineering Cu active sites in 2D materials with porous crystal structures.

KEYWORDS CO_2RR; Cu single-atom catalyst; g-C_3N_4; Methane; CH_4/C_2H_4 ratio

Minhan Li and Fangzhou Zhang contributed equally to this work.

✉ Yuanyuan Ma, yyma@dhu.edu.cn; Jianping Yang, jianpingyang@dhu.edu.cn

1 Institute of Functional Materials, State Key Laboratory for Modification of Chemical Fibers and Polymer Materials, College of Materials Science and Engineering, Donghua University, Shanghai 201620, People's Republic of China
2 College of Materials Science and Engineering, Zhengzhou University, Zhengzhou 450001, People's Republic of China
3 School of Mechanical, Medical and Process Engineering, School of Chemistry and Physics, Queensland University of Technology, 2 George Street, Brisbane, QLD 4001, Australia

1 Introduction

Cu-based electrocatalysts have received extensive attentions for CO_2 electrochemical reduction reaction (CO_2RR), because of their unique ability to convert CO_2 into high-value deep reduction products [1–5]. Motivated by the great CO_2-to-CO performance in CO_2RR obtained on various carbon-supported single-atom catalysts, such as Ni [6–8], Fe [9, 10], Co [11, 12], and Zn [13], the Cu single-atom catalysts (Cu-SACs) have also been investigated for CO_2RR [14]. Similar to the nanostructured Cu-based materials [15], the reported Cu-SACs also exhibited selectivity characteristics toward various reduction products in CO_2RR, including CO [16], CH_4 [17, 18], CH_3OH [19, 20], C_2H_5OH [21, 22], and CH_3COCH_3 (acetone) [23]. The isolated Cu single atoms are usually regard as the main active centers for CO_2RR, and the coordination environment and density of the atomic Cu species play a key role in the selectivity of the Cu-SACs. Cai and co-workers reported that carbon dots-supported Cu-SACs with unique $Cu-N_2O_2$ sites enabled efficient CO_2RR to CH_4 [24]. Xu and co-workers found that O atom coordinated single Cu atoms supported on carbon underwent a reversible transition between atomic sites and Cu_n clusters under CO_2RR condition, and the later catalyzed CO_2 into ethanol [21]. Zheng and co-workers reported that the distance between the atomic $Cu-N_x$ sites was critical for the selectivity between CH_4 and C_2H_4, where the neighboring $Cu-N_x$ sites promoted the C–C coupling and decreased the CH_4/C_2H_4 ratio [25]. During the synthesis of Cu-SACs, however, a high-temperature pyrolysis process is often involved, resulting in poorly defined coordination structure and the aggregation of the atomic Cu sites and thus poorer catalytic selectivity and less accessibility of the active sites [15, 26]. Compared to the pyrolytic SACs, molecular catalysts with explicit and tunable structures are more preferred, due to their well-defined and uniform coordination environments [24].

The challenges in preparing more structural stable and well-configured Cu-SACs triggered our interest in searching more suitable catalyst supports to anchor the active single atoms in a stable and well-coordinated environment. Similar to the well-documented graphene single-atom support, graphitic carbon nitride (g-C_3N_4) has a perfect 2D morphology with single atomic thickness to ensure the best accessibility of the active sites. But differently, g-C_3N_4 contains periodic heptazine units and well-defined "nitrogen pots" that consist of six lone pairs from pyridine-like nitrogen atoms among the heptazine units (nitrogen cavities) [27, 28]. The abundant and periodic nitrogen cavities in the g-C_3N_4 framework makes them become perfect anchoring points for incorporating dense metal atoms with defined distance and coordination numbers [29–31]. Various metal-doped g-C_3N_4 catalysts have been investigated for different electrocatalysis processes, such as hydrogen evolution reaction (HER) [32], oxygen evolution and reduction reaction (OER and ORR) [27, 33], nitrogen reduction reaction [34], and even CO_2RR [35]. Specifically, it has been reported that a Cu-C_3N_4 catalyst exhibited strong CO_2 affinity for promoted CO_2 adsorption toward deep reduction for converting CO_2 into high-value hydrocarbons. However, the Faraday efficiencies (FEs) of these deep reduction reactions were very low, and the role of the Cu sites incorporated in g-C_3N_4 framework for CO_2RR remains unclear [36]. Therefore, further efforts in further enhancing the FEs of the Cu-g-C_3N_4 catalytic system together with a clear mechanism understanding are urgently needed.

In this work, a facile thermal polymerization method is employed to synthesize Cu single atoms loaded in g-C_3N_4 catalysts with different site distance and coordination environments (denoted as Cu_x-CN) for CO_2RR by adjusting the ratios of Cu to g-C_3N_4 in the precursors during the preparation. The synthesis–structure–activity analysis of Cu_x-CN catalysts demonstrated that the Cu single atoms anchored in the nitrogen cavities of g-C_3N_4 are highly active and selective for the production of CH_4. For the $Cu_{0.05}$-CN catalyst with a coordination of N atoms in nitrogen cavities and a chemical state of dominant Cu^+, the most optimal Cu-CN catalyst, presented the highest activity and CH_4 FE (49.04%) and reached 7.97 mA cm^{-2} at -1.2 V_{RHE} with a high CH_4/C_2H_4 ratio of 9, which, to the best knowledge of authors, is the best CO_2-to-CH_4 performance on g-C_3N_4-supported catalysts for CO_2RR. Combining experimental evidence and density functional theory (DFT) calculations, it is revealed that one Cu single atom in one nitrogen cavity and coordinated with 4 N atoms of g-C_3N_4 exhibit a preferred CH_4 catalytic pathway than the C_2H_4 pathway, while the preferred pathway is reversed after forming an adjacent O-coordinated Cu atom. The coordination environment regulated Cu_x-CN catalysts for high-efficiency CH_4 production provide a feasible way to fabricate single-atom Cu active sites for efficient

and selective CO_2RR catalysis and offer some insights into the design of future electrocatalysts.

2 Experimental Section

2.1 Materials

Dicyandiamide (DCDA), copper (II) acetylacetonate $(Cu(acac)_2)$, Iron (III) acetylacetonate $(Fe(acac)_3)$, and nickel (II) acetylacetonate $(Ni(acac)_2)$ were purchased from Sinopharm Chemical Reagent Co., LTD. Potassium bicarbonate (ACS, 99.7–100.5%) and deuterlum oxide $(D_2O, 99.9$ atom% D) were purchased from Shanghai Aladdin Biochemical Technology Co., Ltd. Nafion solution (5 wt% in mixture of lower aliphatic alcohols and water) was purchased from Sigma-Aldrich. Nafion 117 membrane was purchased from Shanghai Hesen Electric Co., LTD. Standard liquid products: methanol ($> 99.9\%$), sodium formate (99.99%), ethanol ($> 99.8\%$ for GC), and n-propanol (99.99%) were purchased from Shanghai Macklin Biochemical Co., Ltd. Deionized water (18.2 MΩ cm^{-2}) was used in this work. The gas products, including H_2, CO, CH_4, and C_2H_4, were calibrated using standard mixed gases purchased from Dalian Special Gases Co., LTD.

2.2 Preparation of Catalysts

To synthesis Cu_x-CN catalysts, 1 g of DCDA and certain amount of $Cu(acac)_2$ were well mixed in a mortar with the mass ratio of $Cu(acac)_2$ to DCDA of x (x = 0.01, 0.05, 0.2, and 0.5 in this work). The well-mixed and grinded powder in a quartz boat was placed in the middle of a tubular furnace. Then the calcination process starts from room temperature to 550 ℃ at 5 ℃ min^{-1} and holds at 550 ℃ for 4 h in Ar atmosphere. After cooling to room temperature, the product was grinded into fine powder. CN sample was prepared by the same procedure except for the absence of $Cu(acac)_2$. Ni_x-CN and Fe_x-CN materials were synthesized by the same method using $Ni(acac)_2$ and $Fe(acac)_3$ as the metal sources.

In order to leach out the Cu in $Cu_{0.05}$-CN catalyst for comparison, the $Cu_{0.05}$-CN catalyst was washed with 1.0 M nitric acid for 12 h at room temperature. After washing with deionized water to neutral pH, the sample that labeled as 0.05-CN was obtained, in which almost all of the Cu metal was removed by acid treatment (Table S1).

2.3 Characterization of Materials

Transmission electron microscope (TEM) images were acquired using JEOL 2100F operated at 200 kV. High-angle annular dark-field scanning transmission electron microscopy (HAADF-STEM) and elemental mapping analysis were performed on Talos F200S operated at 200 kV. Powder X-ray diffraction (XRD) was obtained on Bruker D2 Phaser with a 2θ ranging from 10° to 90° using a Cu Ka X-ray. X-ray photoelectron spectroscopy (XPS) measurements were taken on Escalab 250Xi device. ^1H nuclear magnetic resonance (NMR) spectra were collected on Bruker AVANCE III 600 MHz nuclear magnetic resonance spectrometer. Solid-state ^{13}C magic angle spinning nuclear magnetic resonance (MAS NMR) spectra were acquired with a Bruker AVIII400 spectrometer with a 4 mm MAS BB-1H probe at frequency of 100.63 MHz. Elemental analysis (EA) was performed with Elmentar Vario EL III elemental analyzer to quantitatively determine the elemental content of C, H, and N. Fourier transform infrared (FTIR) spectrum was measured with a Nicolet 6700 FTIR spectrophotometer in the range of 400–4000 cm^{-1} using KBr pellet technique. Spherical aberration-corrected transmission electron microscope (AC-TEM) was performed on Themis ETEM (Thermo Fisher Scientific) transmission electron microscope. The measurements of X-ray absorption spectroscopy (XAS) at the Cu K-edge containing the X-ray absorption near-edge structure (XANES) and extended X-ray absorption fine structure (EXAFS) were taken at the beamline BL14W1 of Shanghai Synchrotron Radiation Facility (SSRF), China. The data processing of XAS measurements was performed using the Demeter software package. Nitrogen sorption–desorption measurements were taken at Micromeritics ASAP2046 machine. Before the measurements, the samples were degassed in a vacuum at 180 °C for at least 10 h. The Brunauer–Emmett–Teller (BET) method was utilized to calculate the specific surface areas using the adsorption data at $P/P_0 = 0.02$—0.20. The pore size distribution was calculated from the adsorption branch by using the Barrett–Joyner–Halenda (BJH) model.

Electrochemical in situ attenuated total reflection Fourier transform infrared (ATR-FTIR) reflection spectroscopy was investigated on a Fourier transform infrared spectrometer (FTIR, Nicolet iS50, Thermo Fisher Scientific) equipped with a liquid nitrogen-cooled mercury cadmium tellurid (MCT) detector. The measurement was conducted in a homemade

electrochemical cell equipped with a Pt-mesh and an Ag/AgCl as counter and reference electrodes, respectively. An Au-coated Si crystal loaded with catalysts was embed into the bottom of the cell to serve as the working electrode. CO_2-saturated 0.1 M $KHCO_3$ is used as the electrolyte for the in situ ATR-FTIR measurement, during which CO_2 gas is continuously bubbled. Chronoamperometry is used for the in situ CO_2RR test, and the spectrum is collected by 32 scans with 4 cm^{-1} resolution. All spectra were subtracted with the background.

2.4 Electrode Preparation

Cu_x-CN catalyst (1 mg) and carbon black (0.25 mg) were dispersed in methanol solution (190 uL). Subsequently, 10 uL of Nafion (5 wt%) was added, followed by ultrasonication for at least 1 h. Then 6 uL catalyst ink was dropped onto a L-type glass carbon electrode with a diameter of 4 mm (geometric area: ~ 0.1256 cm^2) using a pipette and dried under ambient air. The catalyst loading was about 0.24 mg cm^{-2}. The catalysts were electrochemically activated in CO_2-saturated 0.1 M $KHCO_3$ solution by CV (10 scans) from − 0.5 to -1.5 V_{RHE}.

2.5 Electrochemical Reduction of CO_2

CO_2 electrolysis was carried out in a gastight, custom-made two-compartment cell, in which the working electrode was separated from the counter electrode by a Nafion 117 membrane. Ag/AgCl (saturated KCl) was used as the reference electrode, and the three-electrode setup was connected to a potentiostat (Biologic VMP3). A 0.1 M $KHCO_3$ electrolyte solution was used for all CO_2RR tests, and the electrolyte in the cathodic compartment was stirred at a constant rate of ~ 300 rpm during electrolysis. Before CO_2RR, the catholyte was bubbled with CO_2 (99.99%) for 30 min to reach saturation, and CO_2 was kept purging into the cathodic compartment at 10 sccm with stirring at ~ 500 rpm during the CO_2RR. To determine the Faradaic efficiencies (FEs) of the reduced products, chronoamperometry was performed for 1 h at constant iR-corrected potentials. For the long-term stability test, the CO_2-saturated 0.1 M $KHCO_3$ electrolyte was extracted and replaced every 4 h to determine the liquid products. The FEs of gas products were calculated and recorded when the FEs were stable during the last 3 h.

All potentials were measured against an Ag/AgCl reference electrode (3.5 M KCl, stored in a 3.5 M KCl solution before and after use) and converted to the reversible hydrogen electrode (RHE) scale by

$$E_{RHE} = E_{Ag/AgCl} + 0.2046 + 0.059 \times pH \qquad (1)$$

The resistance between the reference and working electrodes was measured by potential electrochemical impedance spectroscopy (PEIS) and the ohmic drop was compensated automatically by the software (80%) and the rest 20% remained uncompensated. All the potentials in the text were iR-corrected if not otherwise specified. Generally, the value of resistance (R) was about 110–115 Ω in CO_2-saturated 0.1 M $KHCO_3$.

2.6 Analysis of Gas and Liquid Products

Gas products from the cathodic compartment during CO_2RR were analyzed using a GC-2014 (Shimadzu) equipped with a TCD detector and two FID detectors, one of which was coupled with a methanizer to detect CO concentration. High-purity Ar (99.999%) was used as the carrier gas. The calibration curves of gas and liquid products can be referred to our previous publication [3].

The Faradaic efficiencies of the gas products were calculated by the GC data using the following equation:

$$FE_g = \frac{Q_g}{Q_{total}} \times 100\% = \frac{\frac{v}{60 \text{ s/ min}} \times \frac{y}{24.5 \text{ L/mol}} \times n \times F}{j_{averge}} \times 100\%$$

$$(2)$$

where v is gas flow rate measured by a flowmeter (Beijing FLOWS instruments Co, Ltd), which is 10 sccm for all the tests, y the measured volumetric content of the gas product, n the number of electrons required to form the gas products, and n = 2, 2, 8, and 12 for H_2, CO, CH_4, and C_2H_4, respectively, F the Faraday constant (96,485 C mol^{-1}), and j the average current density.

Liquid products were analyzed by a 600 MHz NMR spectrometer (Bruker Avance 3 HD 600 MHz) using a presaturation technique to suppress water peak. To take ^1H NMR measurement, 800 uL of electrolyte sampled after CA or stability tests was mixed with 100 uL DMSO standard solution (100 ppm) and 100 uL D_2O. The faradaic efficiencies of liquid products were calculated as follows:

$$FE_l = \frac{Q_l}{Q_{total}} \times 100\% = \frac{n_l \times n \times F}{Q_{total}} \times 100\% \qquad (3)$$

where n_l is the total content of certain liquid products in the catholyte, which was calculated by the concentration and the volume of the catholyte (45 mL), and n is the number of electrons required to form the liquid products, and n = 2, 6, 8, 12, and 18 for formate, methanol, acetate, ethanol, and 1-propanol, respectively.

2.7 Computational Details

We carried out all the DFT calculations in the Vienna ab initio simulation (VASP5.4.4) code [37]. The exchange–correlation is simulated with PBE functional, and the ion–electron interactions were described by the PAW method [38, 39]. The vdWs interaction was included by using empirical DFT-D3 method [40]. The Monkhorst–Pack-grid-mesh-based Brillouin zone k-points are set as $3 \times 3 \times 1$ for all periodic structure with the cutoff energy of 450 eV. The convergence criteria are set as 0.025 eV A^{-1} and 10^{-4} eV in force and energy, respectively. A 20 Å vacuum layer along the z direction is employed to avoid interlayer interference.

The free energy calculation of species adsorption (ΔG) is based on Nørskov et al.'s hydrogen electrode model [41].

$$\Delta G = \Delta E + \Delta E_{ZPE} - T\Delta S \tag{4}$$

Herein ΔE, ΔE_{ZPE}, and ΔS, respectively, represent the changes of electronic energy, zero-point energy, and entropy that caused by adsorption of intermediate. The entropy of $H^+ + e^-$ pair is approximately regarded as half of H_2 entropy in standard condition [42].

3 Results and Discussion

### 3.1 Synthesis and Characterizations of Cu$_x$-CN Catalysts

The single Cu atoms anchoring in the nitrogen cavities of g-C$_3$N$_4$ catalysts with tailoring Cu coverage and coordination (Cu$_x$-CN) were synthesized via an in situ thermal polymerization method by using dicyandiamide (DCDA) and copper (II) acetylacetonate (Cu(acac)$_2$) as precursors for g-C$_3$N$_4$ host and Cu active species, respectively (Fig. 1a). In the synthesis, Cu(acac)$_2$ and DCDA with a mass ratio of x (x = 0.01, 0.05, 0.2, and 0.5) in Cu$_x$-CN catalysts were mixed and then calcined under N$_2$ at 550 °C to obtain the

Cu$_x$-CN catalysts. The pure g-C$_3$N$_4$ (denoted as CN) is yellowish powders. With the increase in Cu contents in Cu$_x$-CN catalysts, the color gradually turns into dark brown (Fig. 1a).

The morphology of the catalysts and the dispersion state of Cu species are first characterized. The TEM and high-angle annular dark-field scanning transmission electron microscopy (HAADF-STEM) images of both the CN and the Cu$_x$-CN catalysts (Figs. 1b and S1-S2) confirm their stacking layered structures and exclude the existence of crystalline or aggregated Cu species in these catalysts. The stacked layers gradually became fragmentary with the increasing Cu content in Cu$_x$-CN catalysts, demonstrating the increasing surface area and pore structure. Thus, the as-prepared material is investigated by the N$_2$ adsorption–desorption measurements. As expected, after loading Cu the surface area and porosity of Cu$_x$-CN catalysts increase significantly as compared with the pristine CN sample (Fig. S3). As observed on the Cu$_{0.05}$-CN catalyst by aberration-corrected HAADF-STEM, the bright dots scatteringly distribute in the g-C$_3$N$_4$ host, indicating the presence of isolated Cu atoms in the catalyst (Fig. 1c). Interestingly, even at high Cu contents, isolated Cu atoms appeared at a high density rather than forming crystalline species or aggregated clusters, for example, in the Cu$_{0.5}$-CN catalysts (Fig. S2c), which is consistent with the TEM results. The uniform distribution of Cu, C, N, and O elements in the Cu$_{0.05}$-CN catalyst is further verified by the elemental mappings (Figs. 1d and S4). The high density of the atomic sites shortens the distance between single atoms, which may impact on both the activity and the selectivity of the catalysts [25, 43]. Besides, this facile strategy can be extended to other transition metals to form g-C$_3$N$_4$-supported single metal atoms, such as Ni and Fe (Figs. S5-S6).

The XRD patterns of the CN, the Cu$_{0.01}$-CN, and the Cu$_{0.05}$-CN catalysts exhibit the (100) and (002) peaks of g-C$_3$N$_4$ appeared at 13.0° and 27.2°, corresponding to the repeating in-plane melem units and the stacking of graphite-like layer structure, respectively (Fig. 2a) [28]. For the Cu$_{0.2}$-CN and Cu$_{0.5}$-CN catalysts, the intensity of (002) peak decreased and the (100) peak disappeared, indicating the loss of periodical repeatability of the in-plane melem units in these two catalysts. No phase of Cu species appeared in all catalysts, which excludes the existence of crystalline Cu species and indicates the likely chemically coordination of Cu into the g-C$_3$N$_4$ host in the form of Cu-N$_y$ structure (y is the coordinated N number) [28]. The FTIR spectra of all
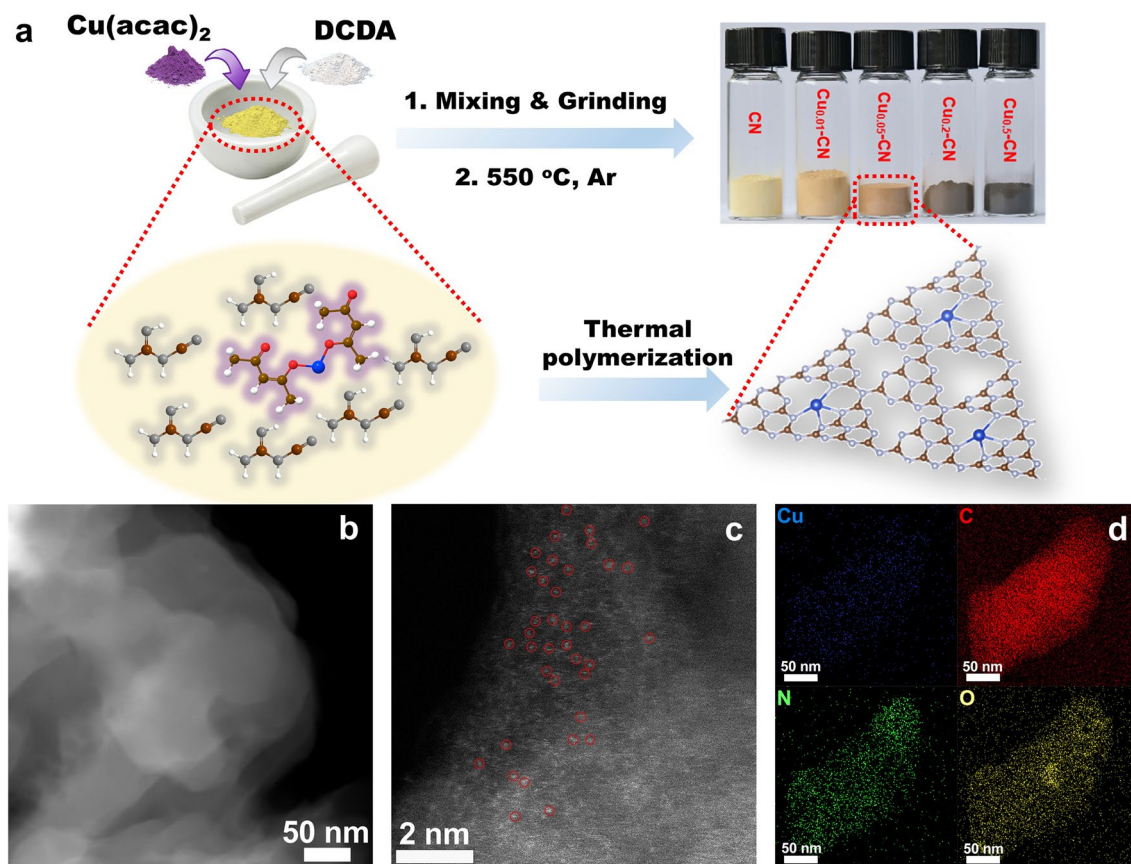
Fig. 1 a Schematic illustration of the synthesis of Cu_x-CN catalysts and the optical photographs of the as-synthesized Cu_x-CN catalysts. **b** HAADF-STEM image, **c** aberration-corrected HAADF-STEM image, and **d** EDS mapping of $Cu_{0.05}$-CN catalysts

samples exhibit a broad peak between 3100 and 3600 cm^{-1} that can be attributed to N–H and O–H stretching [44, 45], while the weak peaks appear at ~2176 cm^{-1} can be assigned to the stretching of triple C≡N bond, which is considered as defects within g-C_3N_4 [46]. The increasing intensity of C≡N peaks support the fact that the defect increases with increasing Cu content in Cu_x-CN catalysts. The typical bands of the stretching vibrations of C-N heterocycles and breathing mode of s-triazine units appears in at ~1250–1635 and at ~810 cm^{-1}, respectively [47–49]. Notably, at low Cu loads, these two characteristic FTIR spectra of the $Cu_{0.01}$-CN and $Cu_{0.05}$-CN catalysts are almost identical with that of the pure g-C_3N_4 (Fig. 2b), indicating the well-preserved g-C_3N_4 frameworks. On the contrary, these characteristic bands are significantly weakened in the $Cu_{0.2}$-CN and $Cu_{0.5}$-CN catalysts, indicating the high Cu loads in the catalysts can partially damage of the C-N heterocyclic structure [50]. To further confirm the local structures of the Cu_x-CN catalysts,

solid-state ^{13}C nuclear magnetic resonance (^{13}C NMR) spectra were carried out on the Cu_x-CN with various Cu contents (Fig. 2c). Two distinct peaks at chemical shift of 156.3 and 164.0 ppm, which are assigned to the C atoms connected to different N atoms in C-N heterocycle [49], are observed in the CN, $Cu_{0.01}$-CN, and $Cu_{0.05}$-CN samples, indicating the skeleton structure of g-C_3N_4 are well retained and the introduced Cu atoms are likely to incorporate into the nitrogen cavities among C-N heterocyclic structures in these samples. However, the two peaks dramatically attenuate for the $Cu_{0.2}$-CN and $Cu_{0.5}$-CN catalysts, demonstrating the destruction of g-C_3N_4 framework by increasing $Cu(acac)_2$ content in the preparation. Obviously, the XRD, FTIR, and ^{13}C NMR results explicitly suggest that the basic structure units and framework of the g-C_3N_4 host are well retained for $Cu_{0.01}$-CN and $Cu_{0.05}$-CN catalysts with low Cu loads, which is likely associated with the preferential incorporation of isolated Cu atoms in the nitrogen cavities of g-C_3N_4
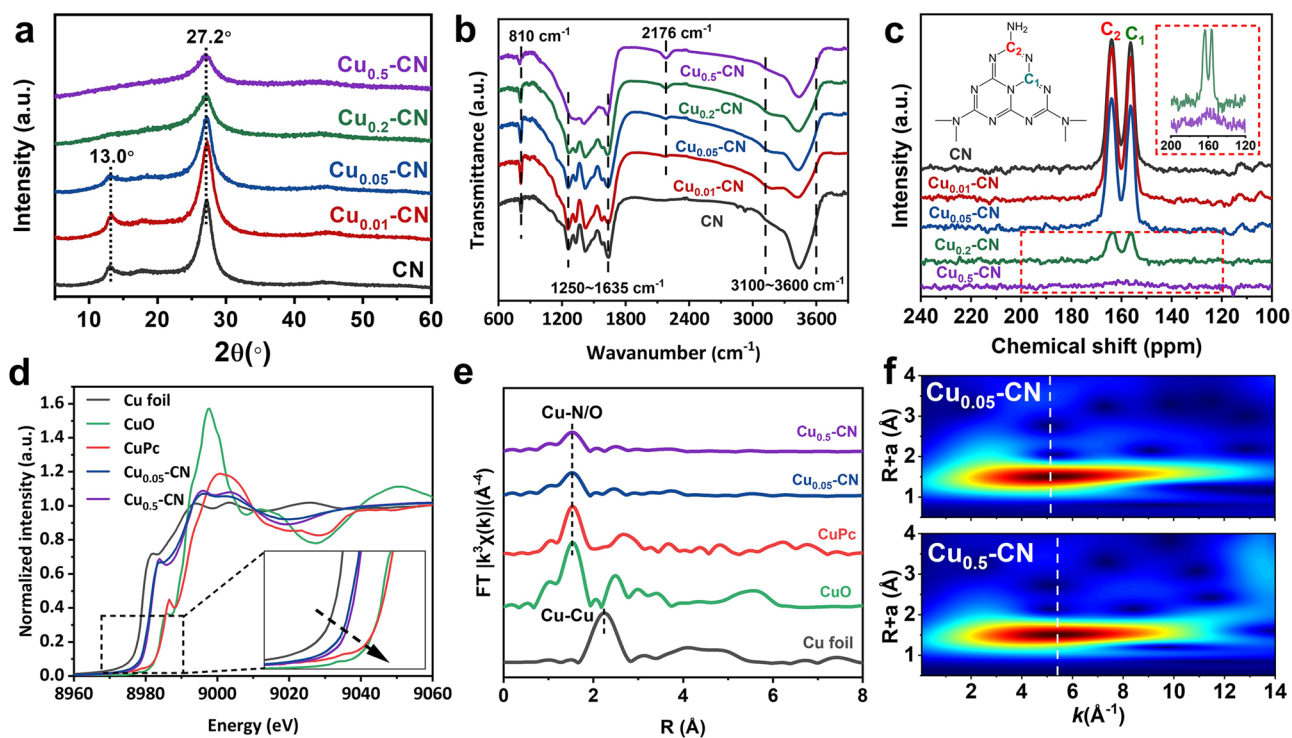
Fig. 2 **a** XRD patterns of Cu_x-CN catalysts. **b** FTIR spectra of Cu_x-CN catalysts. **c** Solid-state ^{13}C NMR spectra of Cu_x-CN catalysts. **d** Cu K-edge XANES spectra of Cu foil, $Cu_{0.05}$-CN, $Cu_{0.5}$-CN, CuPc, and CuO samples. **e** Fourier transform (FT) EXAFS spectra of Cu K-edge of Cu foil, $Cu_{0.05}$-CN, $Cu_{0.5}$-CN, CuPc, and CuO samples. **f** Wavelet transform (WT) of $Cu_{0.05}$-CN and $Cu_{0.5}$-CN catalysts

with Cu–N structures. On the other hand, the destructed C-N heterocycles and g-C_3N_4 framework of $Cu_{0.2}$-CN and $Cu_{0.5}$-CN catalysts indicate the changed atomic coordination at relatively high Cu loads.

To get a clearer understanding on the chemical states and coordination of Cu atoms in the Cu_x-CN catalysts, XAFS measurements were taken together with Cu foil, copper (II) phthalocyanine (CuPc), and CuO as references. As illustrated by the X-ray absorption near-edge structure (XANES) in Fig. 2d, the positions of Cu K-edge for the $Cu_{0.05}$-CN and $Cu_{0.5}$-CN catalysts are close, which are located between the Cu K-edge edges of Cu foil and CuO. The average oxidation states of Cu in the $Cu_{0.05}$-CN and $Cu_{0.5}$-CN catalysts are found to be close to +1 by fitting (Fig. S7) [51]. The Fourier transformed extended EXAFS spectra with k^3-weight of $Cu_{0.05}$-CN, $Cu_{0.5}$-CN, and the references are depicted in Fig. 2e. It is found that the $Cu_{0.05}$-CN and $Cu_{0.5}$-CN catalysts exhibited only one dominating peak around 1.53 Å, which could be assigned to the scattering of either Cu–N or Cu–O coordination [24]. As references, CuO shows a main peak attributed to Cu–O at 1.53 Å while the Cu-Cu coordination in Cu foil

is at 2.24 Å. These results further verify that no Cu-Cu interaction existed but only the isolated Cu atoms in the Cu_x-CN catalysts, even for $Cu_{0.5}$-CN with high Cu loads. Notably, the $Cu_{0.5}$-CN catalyst exhibited a lower intensity at 1.53 Å than that of the $Cu_{0.05}$-CN catalyst, suggesting a possible different coordination environment achieved at higher Cu contents [52, 53]. Due to the great resolution in both k and R spaces, the wavelet transform of Cu K-edge EXAFS spectra were performed to investigate the atomic configuration of $Cu_{0.05}$-CN and $Cu_{0.5}$-CN catalysts (Fig. 2f). summits at 5.2 and 5.4 Å^{-1} were identified for $Cu_{0.05}$-CN and $Cu_{0.5}$-CN, respectively, in the k space. Although the wavelet transform of Cu K-edge EXAFS is unable to discriminate the N and O coordination completely [24], these results confirm the coordination environment of the Cu single atoms in Cu_x-CN can be varied as the variation of Cu loading amounts.

The composition, valence state, and detailed structural and binding information of the Cu_x-CN catalysts were further investigated by various characterizations. To verify the actual Cu contents in each catalyst, inductively coupled plasma–atomic emission spectrometry (ICP-AES) was

employed. It reveals that the actual Cu contents are proportional to the $Cu(acac)_2$ addition amounts, and the $Cu_{0.05}$-CN catalyst had a Cu content of 0.954 wt% (Table S1). The compositions of the CN and Cu_x-CN catalysts were then probed by an elemental analysis (EA). As shown in Fig. 3a, the CN and Cu_x-CN catalysts possess similar C content, while the N and H contents decrease distinctly for the $Cu_{0.2}$-CN and $Cu_{0.5}$-CN catalysts. Similarly, the significant decrease of N content in these two catalysts was also observed by the atomic percentage determined by XPS (Figs. 3b and S8), accompanying with the increases in Cu and O contents. The composition variations indicate that the Cu atoms are

successfully introduced in g-C_3N_4 host accompanied by the introduction of O atoms, which is hypothesized to be caused by the use of oxygen-containing copper salt (copper acetylacetonate) in the polymerization process of g-C_3N_4.

The bonding and chemical states of the elements in CN and Cu_x-CN catalysts are analyzed by the XPS spectra collected on the Cu, C, and N elements of all catalysts. The Cu 2p peaks can be fitted with two peaks (Figs. 3c and S9). The Cu(1) peak at about 932.4 eV is predominant in the $Cu_{0.01}$-CN and $Cu_{0.05}$-CN catalysts and can be ascribed to Cu^0 or Cu^{1+} species, while the Cu(2) peak at about 935.0 eV ascribed to Cu^{2+} species increases
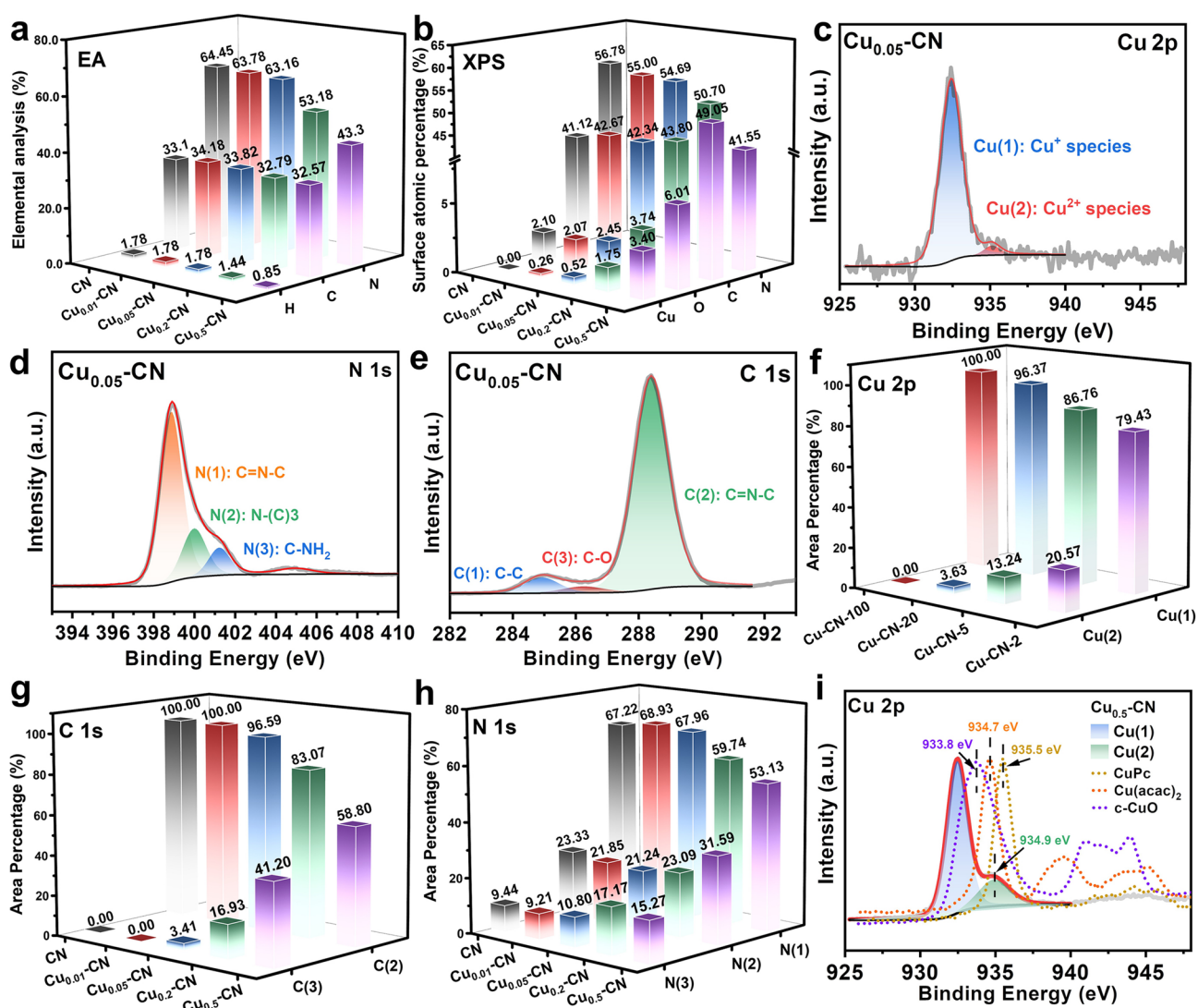
Fig. 3 **a** Elemental analysis of the catalysts. **b** Surface composition of the catalysts determined by XPS. **c–e** Peak fitting of Cu 2p, N 1s, and C 1s spectra of the $Cu_{0.05}$-CN catalyst. **f–h** Peak fitting summary of Cu 2p, C 1s, and N 1s spectra of the catalysts. **i** Comparison of Cu 2p spectra of the $Cu_{0.5}$-CN catalyst with other cupric compounds

significantly in the $Cu_{0.2}$-CN and $Cu_{0.5}$-CN catalysts with higher Cu contents (Fig. S6d-e). Further, according to the XANES results and the Cu LMM Auger spectra of Cu_x-CN catalysts, it can be concluded that Cu(1) peaks in Cu_x-CN should be ascribed to Cu^{1+} species, as the overwhelming Cu^{1+} peaks and negligible Cu^0 peaks in the Cu LMM spectra (Fig. S9f) [54]. The N 1s spectra can be deconvoluted into three states of N(1), N(2), and N(3) at about 398.7, 399.8, and 401.1 eV, respectively (Figs. 3d and S10), as well as a small peak at 404.9 eV, which corresponds to the π-excitation. The N(1), N(2), and N(3) peaks can be attributed to the sp^2 hybridized nitrogen in C-N heterocycles (C＝N–C), the tertiary N (N-(C)3), and the N in amino functional groups (C-NH_2), respectively [55]. The C 1s peaks can also be fitted with three peaks denoted as C(1), C(2), and C(3) at about 284.8, 288.3, and 286.6 eV, respectively (Figs. 3e and S11). The C(1) peak can be ascribed to graphitic carbon and used for calibration. The C(2) peak is the main component of C 1s spectra for all catalysts, which should be the C atoms in the C-N heterocycles (C＝N–C). The C(3) state gradually emerges and rises with the increase of Cu contents in Cu_x-CN catalysts, which may attribute to the C in a C-O structure [55–57].

The fitting results of the Cu 2p, C 1s, and N 1s spectra are summarized in Fig. 3f-h. In accordance with the structural characterization of the catalysts in Fig. 2, the fitting results show that the species and ratio of C and N are almost unaffected for the $Cu_{0.01}$-CN and $Cu_{0.05}$-CN catalysts. Combined the results of XAFS measurements, it is reasonable that the isolated Cu atoms preferentially embed nitrogen cavities to form Cu–N coordination structures with little effects on the C-N heterocyclic structure in these two catalysts. However, with the increasing addition of $Cu(acac)_2$ in the preparation, the significantly reduced N(1) and C(2) peaks further confirm the destruction of the C-N heterocyclic structure of the g-C_3N_4 host in the $Cu_{0.2}$-CN and $Cu_{0.5}$-CN catalysts. Meanwhile, the concurrent increases of the Cu(2) species and the O atomic ratio for the $Cu_{0.2}$-CN and $Cu_{0.5}$-CN catalysts imply the emerging Cu^{2+} species is related to the increasing C-O structures, which is evidenced by increased C(3) peaks and the O 1s spectra (Figs. 3g and S12). Further, by comparing the Cu 2p spectra of the $Cu_{0.5}$-CN catalyst with some references, including commercial CuO powder, $Cu(acac)_2$, and CuPc, it is found that the binding energy of Cu^{2+} species in the $Cu_{0.5}$-CN catalyst is close to $Cu(acac)_2$

(Fig. 3i), indicating the structure of the emerging Cu^{2+} sites in the $Cu_{0.2}$-CN and $Cu_{0.5}$-CN catalysts are likely the O-coordinated structure [58]. Therefore, the possible evolution of the atomic configurations of the Cu_x-CN catalysts can be drawn from the above analysis. In the $Cu_{0.01}$-CN and $Cu_{0.05}$-CN catalysts, the atomic Cu sites predominantly embed in the nitrogen cavities of the g-C_3N_4 host, forming Cu–N coordination without affecting its framework structure. However, in the $Cu_{0.2}$-CN and $Cu_{0.5}$-CN catalysts, the O-coordinated Cu species emerge substantially accompanied with the partial destruction of the C-N heterocycles and g-C_3N_4 framework.

3.2 Catalytic Performance of CO_2RR

The CO_2RR performance of the CN and Cu_x-CN catalysts was evaluated in a H-cell with 0.1 M $KHCO_3$ as the electrolyte. The potential dependent FE of different products on the CN and Cu_x-CN catalysts was collected by a chronoamperometry test of 1 h in the potential range from -0.9 to -1.3 V_{RHE} (Fig. 4a). The gaseous products account for the major reduction products on all catalysts (Figs. 4b and S13-S14). Compared with the pristine g-C_3N_4, the Cu_x-CN catalysts exhibited higher activity and selectivity toward CH_4 in the tested potential range. The highest FE of 49.04% at -1.2 V_{RHE} for CH_4 reached on the $Cu_{0.05}$-CN catalyst with a CH_4 current density of 7.97 mA cm^{-2}, which further increased to 9.78 mA cm^{-2} at -1.3 V_{RHE} (Fig. 4c-d). Although the CN catalyst also exhibits certain activity toward CO_2RR in the potential range, it only shows quite low CH_4 activity and selectivity with a maximum CH_4 current density of 2.11 mA cm^{-2} at -1.3 V_{RHE}. Clearly, the enhanced CH_4 production obtained on the Cu_x-C_3N_4 catalysts indicates the incorporated Cu sites in these catalysts are active sites for CO_2RR catalysis. Probably contributed by the stable configuration of single Cu atoms in the $Cu_{0.05}$-CN catalysts (Fig. S15), the catalytic stability up to 10 h of continuous CO_2RR test was performed on the $Cu_{0.05}$-CN catalyst at -1.2 V_{RHE}, which showed a slight decrease within the stability test (Fig. 4e).

To gain further insight into the improved CH_4 activity and selectivity and elucidate the role the atomic Cu sites in the $Cu_{0.05}$-CN catalyst, temperature-programmed CO desorption and control experiments were carried out. The larger desorption peak area and stronger chemisorption of CO on
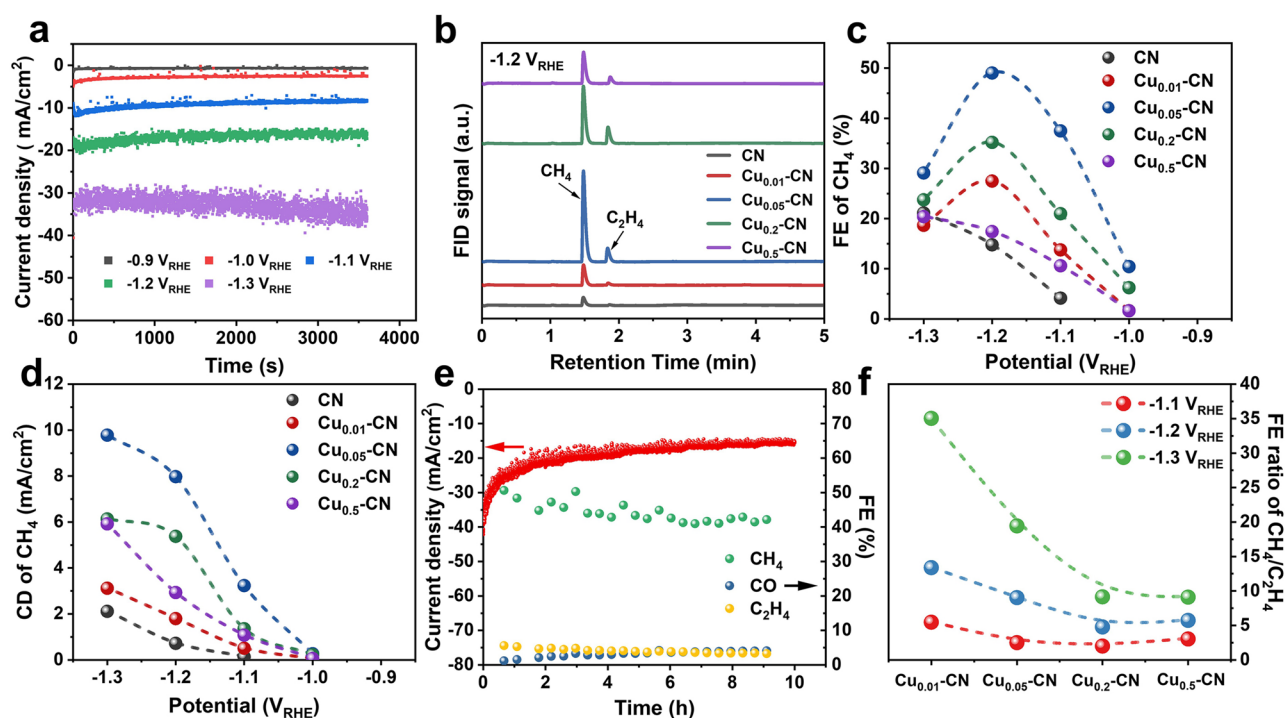
Fig. 4 CO_2RR performance of CN and Cu_x-CN catalysts. **a** Typical chronoamperometry curves at different potentials on $Cu_{0.05}$-CN catalysts. **b** FID signals of GC showing the main gaseous CO_2RR products of CH_4 and C_2H_4 on Cu_x-CN catalysts. **c** FE of CH_4 at different potentials on Cu_x-CN catalysts. **d** Current density (CD) of CH_4 at different potentials on Cu_x-CN catalysts. **e** Catalytic stability of $Cu_{0.05}$-CN catalyst during 10 h of CO_2RR test at -1.2 V_{RHE}. **f** FE ratio of CH_4/C_2H_4 on Cu_x-CN catalysts at different potentials

the $Cu_{0.05}$-CN catalyst than CN indicate the increased CO binding sites and enhanced CO binding strength resulted by Cu incorporation (Fig. S16a) [36]. To probe the role of the single Cu atoms for CO_2RR-to-CH_4, the $Cu_{0.05}$-CN catalyst was washed by 1.0 M nitric acid for 12 h at room temperature to obtain 0.05-CN sample and the almost all of the Cu metal was removed by acid treatment (Table S1). Compared with the $Cu_{0.05}$-CN catalyst, the 0.05-CN catalyst exhibits much lower current density without CH_4 product at -1.2 V_{RHE} (Fig. S16b-c). In addition, the effect of carbon black in the preparation of catalysts ink on the CO_2RR is also excluded (Fig. S16d). Therefore, it is believed that the high CO_2RR-to-CH_4 activity and selectivity on the $Cu_{0.05}$-CN catalyst are originated from the single Cu sites embedded into the nitrogen cavities in the g-C_3N_4 host. However, it should be noted that the semiconductor characteristic of g-C_3N_4 host lead to the poor charge transfer ability of the Cu_x-CN catalysts, although the charge transfer resistance of CN can be reduced slightly by Cu doping (Fig. S17) [30]. Therefore, improving the conductivity may be a promising

for further boosting the CO_2RR performance of Cu_x-CN catalysts.

3.3 Discussions

It has been reported that the isolated Cu sites tended to convert CO_2 into C_1 products in CO_2RR, such as CO, CH_4, and CH_3OH [16, 19, 25, 59]. On the other hand, the C_{2+} products could also be obtained on Cu single-atom catalysts if the atomically dispersed Cu reversibly transformed into clusters or nanoparticles under reaction conditions or additional active centers acted collaboratively with single Cu sites [21, 22]. Furthermore, the density of Cu sites and their distance played a key role in the selectivity between the CH_4 and the C_2H_4 products and the ratio of CH_4/C_2H_4 as the adjacent Cu-N_2 sites enabled the C–C coupling, which is prerequisite for C_2H_4 formation [25]. Given two types of controllable and adjustable Cu sites in the Cu_x-CN catalysts in this work, the FE ratios of CH_4/C_2H_4 on

Cu_x-CN catalysts are compared at different potentials. As shown in Fig. 4f, the FE ratio of CH_4/C_2H_4 increased with the decrease of potentials for all catalysts. The $Cu_{0.01}$-CN catalyst with the lowest Cu content and exclusive single-atom Cu sites shows the highest FE ratio of CH_4/C_2H_4 of 35.03 at -1.3 V_{RHE}. Such high FE ratio of CH_4/C_2H_4 outperforms most reported results (Fig. S18), which is suggested to ascribed to the highly selective toward CH_4 of the single Cu atomic sites in nitrogen cavities and the long distance between these sites of the $Cu_{0.01}$-CN catalyst with low Cu load. The $Cu_{0.05}$-CN catalyst shows a CH_4/C_2H_4 FE ratio of 9.03 at -1.2 V_{RHE}, at which the highest FE of CH_4 is achieved. The decreased CH_4/C_2H_4 FE ratio on the $Cu_{0.05}$-CN catalyst is hypothesized to be resulted from the shortened distance between single Cu atoms at increasing Cu loads and the small amount of Cu^{2+} species in the $Cu_{0.05}$-CN catalyst [25]. Therefore, the high CH_4/C_2H_4 FE ratio on the $Cu_{0.01}$-CN catalyst and the outstanding CO_2RR-to-CH_4 performance on the $Cu_{0.05}$-CN catalyst support the hypothesis that the single Cu atoms embedded into the nitrogen cavities of the g-C_3N_4 host are active sites for CH_4 formation.

To explore the reaction mechanism of the CO_2RR on Cu_x-CN catalysts, in situ ATR-FTIR measurements were taken to identify the key intermediates during CO_2RR in a homemade cell (Fig. S19). As shown in Fig. 5a, the peaks at 1268 and 1350 cm^{-1} can be ascribed to the *COOH intermediate, which is generally considered as the key intermediate for CO_2 electrochemical conversion to CO and further reduction [60]. Notably, the signals at 1130 and 1490 cm^{-1}, which can be assigned to *CH_2O and *CH_3O, respectively [61], intensify as the potentials decreased from -1.0 V_{RHE} to -1.2 V_{RHE}. Therefore, the formation of CH_4 on $Cu_{0.2}$-CN catalysts is likely through the proton–electron transfer of *COOH, *CO, *CHO, *CH_2O, and *CH_3O in succession [60, 62].

To gain a comprehensive insight into the formation of atomic Cu sites and the structure–activity relationship of Cu_x-CN catalysts, DFT calculations were then performed. Previously, both experimental and theoretical studies have demonstrated that the nitrogen cavity consists of six nitrogen atoms in g-C_3N_4, which is the prevailing and stable structure for accommodating single metal atoms [36, 63]. The calculation also shows that the formation energy of a Cu atom incorporated in one nitrogen cavity of g-C_3N_4 (Cu_1-g-C_3N_4) is -2.11 eV (Fig. 5b),

which is far less than that for forming two Cu atoms into one cavity (Cu_2-g-C_3N_4). Furthermore, the experimental EXAFS spectrum can be fitted with great accuracy using Cu_1-g-C_3N_4 model, giving the average bond length R of 1.92 Å and the coordination number N of about 3.3 for Cu–N bond (Fig. S20 and Table S2). The optimized structure shows that the incorporated Cu atom coordinates with four N atoms in the nitrogen cavities and the charge transfer occurs from Cu to N atoms (Fig. S21). The calculated free energy profile demonstrates that the rate determining step (RDS) for the conversion of CO_2-to-CH_4 is *CO → *CHO with a ΔG of 1.09 eV on the Cu_1-g-C_3N_4 single active site, which is about 0.14 eV lower than the ΔG of RDS of the C_2H_4 pathway (Fig. 5c). Therefore, it is more energy favorable to form CH_4 rather than other hydrocarbons on single Cu atomic sites hosted by g-C_3N_4. Based on the experimental observation, which shows the destructed g-C_3N_4 structure and the increasing O-coordinated Cu atoms in the Cu_x-CN catalysts with increasing Cu loads, the model of Cu_2-d-C_3N_4 consisted of adjacent Cu sites and damaged C-N heterocycles is built (Fig. S22). The free energy barrier of the RDS for the CH_4 pathway is 0.11 eV higher than that for the C_2H_4 pathway on the dual-site Cu_2-d-C_3N_4 (Fig. S23). According to the free energy differences between CH_4 and C_2H_4 pathways (Fig. 5d), it is concluded that the CH_4 pathway prevails over the C_2H_4 pathway on single Cu atomic sites in nitrogen cavities of g-C_3N_4, while the trend reverses on dual Cu sites on destructed g-C_3N_4 host. Therefore, the emergence of adjacent O-coordinated Cu sites in the Cu_x-CN catalysts with high Cu loads suppresses the CH_4 formation but facilitates the production of C_2H_4, as observed in experiments. Based on the mechanism and theoretical study, the CO_2-to-CH_4 pathway on the favorable Cu sites is proposed to proceed via the intermediates of *COOH, *CO, *CHO, *CH_2O, and *CH_3O (Fig. 5e).

4 Conclusions

In this work, structurally stable single Cu atoms embedded in the nitrogen cavities of g-C_3N_4 frameworks have been successfully synthesized with controlled configurations and chemical states to catalyze CO_2RR for CH_4 production. High CH_4 activity and selectivity and high FE ratio of CH_4/C_2H_4 were achieved on the $Cu_{0.01}/Cu_{0.05}$-CN catalysts with
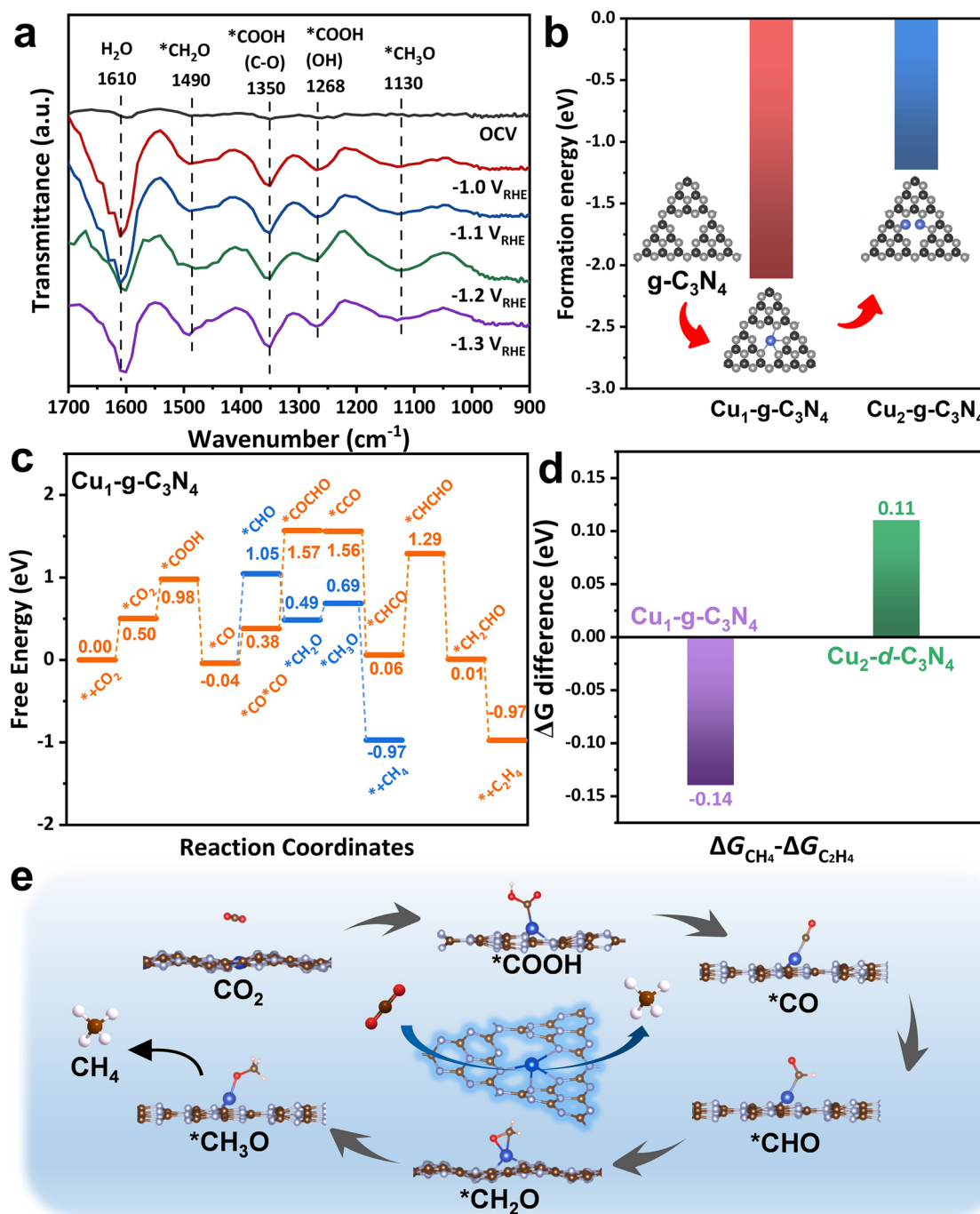
Fig. 5 Mechanism and theoretical study. **a** In situ ATR-FTIR spectra of $Cu_{0.05}$-CN catalysts at decreasing potentials in a CO_2-saturated 0.1 M $KHCO_3$ electrolyte. **b** Calculated formation energies of single and dual Cu sites in the nitrogen cavity of g-C_3N_4. **c** Free energy diagram of CO_2 to CH_4 and C_2H_4 on Cu_1-g-C_3N_4. **d** Difference of free energy barriers between CH_4 and C_2H_4 pathways on Cu_1-g-C_3N_4 and Cu_2-d-C_3N_4. **e** Proposed reaction pathway of CH_4 formation on Cu_1-g-C_3N_4

predominant single Cu atomic sites. The increase of Cu contents in the Cu_x-CN catalysts leads to the emerging of a second O-coordinated Cu sites accompanied with the structural destruction of g-C_3N_4 support, resulting in reduced CH_4

activity and selectivity and thus decreased CH_4/C_2H_4 ratio. This work provides a new strategy for constructing efficient single Cu atom catalysts for the conversion of CO_2-to-CH_4 and delivers some insights into the understanding on the

regulation of Cu-based catalysts for CO_2RR to achieve desired selectivity and products.

Declarations

Electronic supplementary material The online version of this article (https://doi.org/10.1007/s40820-023-01188-1) contains supplementary material, which is available to authorized users.

References

1. H. Xie, T. Wang, J. Liang, Q. Li, S. Sun, Cu-based nanocatalysts for electrochemical reduction of CO_2. Nano Today **21**, 41–54 (2018). https://doi.org/10.1016/j.nantod.2018.05.001

2. A. Vasileff, C. Xu, Y. Jiao, Y. Zheng, S.-Z. Qiao, Surface and interface engineering in copper-based bimetallic materials for selective CO_2 electroreduction. Chem **4**, 1809–1831 (2018). https://doi.org/10.1016/j.chempr.2018.05.001

3. M. Li, Y. Ma, J. Chen, W. Luo, M. Sacchi et al., Residual chlorine induced cationic active species on porous Cu electrocatalyst for highly stable electrochemical co_2 reduction to C_{2+}. Angew. Chem. Int. Ed. **60**, 11487–11493 (2021). https://doi.org/10.1002/anie.202102606

4. Y. Quan, J. Zhu, G. Zheng, Electrocatalytic reactions for converting CO_2 to value-added products. Small Sci. **1**, 2100043 (2021). https://doi.org/10.1002/smsc.202100043

5. M. Li, J.-N. Zhang, Rational design of bimetallic catalysts for electrochemical CO_2 reduction reaction: a review. Sci. China Chem. **66**, 1288–1317 (2023). https://doi.org/10.1007/s11426-023-1565-5

6. Y. Cheng, S. Zhao, B. Johannessen, J.-P. Veder, M. Saunders et al., Atomically dispersed transition metals on carbon nanotubes with ultrahigh loading for selective electrochemical carbon dioxide reduction. Adv. Mater. **30**, e1706287 (2018). https://doi.org/10.1002/adma.201706287

7. H.B. Yang, S.-F. Hung, S. Liu, K. Yuan, S. Miao et al., Atomically dispersed Ni(i) as the active site for electrochemical CO_2 reduction. Nat. Energy **3**, 140–147 (2018). https://doi.org/10.1038/s41560-017-0078-8

8. H. Guo, D.-H. Si, H.-J. Zhu, Q.-X. Li, Y.-B. Huang et al., Ni single-atom sites supported on carbon aerogel for highly efficient electroreduction of carbon dioxide with industrial current densities. eScience **2**, 295–303 (2022). https://doi.org/10.1016/j.esci.2022.03.007

9. J. Gu, C.-S. Hsu, L. Bai, H.M. Chen, X. Hu, Atomically dispersed Fe^{3+} sites catalyze efficient CO_2 electroreduction to CO. Science **364**, 1091–1094 (2019). https://doi.org/10.1126/science.aaw7515

10. C. Zhang, S. Yang, J. Wu, M. Liu, S. Yazdi et al., Electrochemical CO_2 reduction with atomic iron-dispersed on nitrogen-doped graphene. Adv. Energy Mater. **8**, 1703487 (2018). https://doi.org/10.1002/aenm.201703487

11. X. Wang, Z. Chen, X. Zhao, T. Yao, W. Chen et al., Regulation of coordination number over single co sites: triggering the efficient electroreduction of CO_2. Angew. Chem. Int. Ed. **57**, 1944–1948 (2018). https://doi.org/10.1002/anie.201712451

12. Y. Pan, R. Lin, Y. Chen, S. Liu, W. Zhu et al., Design of single-atom $Co-N_5$ catalytic site: A robust electrocatalyst for CO_2 reduction with nearly 100% CO selectivity and remarkable stability. J. Am. Chem. Soc. **140**, 4218–4221 (2018). https://doi.org/10.1021/jacs.8b00814

13. F. Yang, P. Song, X. Liu, B. Mei, W. Xing et al., Highly efficient CO_2 electroreduction on ZnN_4-based single-atom catalyst. Angew. Chem. Int. Ed. **57**, 12303–12307 (2018). https://doi.org/10.1002/anie.201805871

14. D. Xue, H. Xia, W. Yan, J. Zhang, S. Mu, Defect engineering on carbon-based catalysts for electrocatalytic CO_2 reduction. Nano-Micro Lett. **13**, 5 (2020). https://doi.org/10.1007/s40820-020-00538-7

15. M. Li, H. Wang, W. Luo, P.C. Sherrell, J. Chen et al., Heterogeneous single-atom catalysts for electrochemical co_2 reduction reaction. Adv. Mater. **32**, 2001848 (2020). https://doi.org/10.1002/adma.202001848

16. W. Zheng, J. Yang, H. Chen, Y. Hou, Q. Wang et al., Atomically defined undercoordinated active sites for highly efficient co_2 electroreduction. Adv. Funct. Mater. **30**, 1907658 (2019). https://doi.org/10.1002/adfm.201907658

17. Y. Wang, Z. Chen, P. Han, Y. Du, Z. Gu et al., Single-atomic cu with multiple oxygen vacancies on ceria for electrocatalytic CO_2 reduction to CH_4. ACS Catal. **8**, 7113–7119 (2018). https://doi.org/10.1021/acscatal.8b01014

18. Z. Weng, Y. Wu, M. Wang, J. Jiang, K. Yang et al., Active sites of copper-complex catalytic materials for electrochemical carbon dioxide reduction. Nat. Commun. **9**, 415 (2018). https://doi.org/10.1038/s41467-018-02819-7

19. H. Yang, Y. Wu, G. Li, Q. Lin, Q. Hu et al., Scalable production of efficient single-atom copper decorated carbon membranes for CO_2 electroreduction to methanol. J. Am. Chem. Soc. **141**, 12717–12723 (2019). https://doi.org/10.1021/jacs.9b04907

20. Q. Zhao, C. Zhang, R. Hu, Z. Du, J. Gu et al., Selective etching quaternary max phase toward single atom copper immobilized mxene ($Ti_3C_2Cl_x$) for efficient CO_2 electroreduction to methanol. ACS Nano **15**, 4927–4936 (2021). https://doi.org/10.1021/acsnano.0c09755

21. H. Xu, D. Rebollar, H. He, L. Chong, Y. Liu et al., Highly selective electrocatalytic CO_2 reduction to ethanol by metallic clusters dynamically formed from atomically dispersed copper. Nat. Energy **5**, 623–632 (2020). https://doi.org/10.1038/s41560-020-0666-x

22. D. Karapinar, N.T. Huan, N. Ranjbar Sahraie, J. Li, D. Wakerley et al., Electroreduction of CO_2 on single-site copper-nitrogen-doped carbon material: Selective formation of ethanol and reversible restructuration of the metal sites. Angew. Chem. Int. Ed. **58**, 15098–15103 (2019). https://doi.org/10.1002/anie.201907994

23. K. Zhao, X. Nie, H. Wang, S. Chen, X. Quan et al., Selective electroreduction of CO_2 to acetone by single copper atoms anchored on N-doped porous carbon. Nat. Commun. **11**, 2455 (2020). https://doi.org/10.1038/s41467-020-16381-8

24. Y. Cai, J. Fu, Y. Zhou, Y.-C. Chang, Q. Min et al., Insights on forming N, O-coordinated Cu single-atom catalysts for electrochemical reduction C_O2 to methane. Nat. Commun. **12**, 586 (2021). https://doi.org/10.1038/s41467-020-20769-x

25. A. Guan, Z. Chen, Y. Quan, C. Peng, Z. Wang et al., Boosting CO_2 electroreduction to CH_4 via tuning neighboring single-copper sites. ACS Energy Lett. **5**, 1044–1053 (2020). https://doi.org/10.1021/acsenergylett.0c00018

26. X. Li, H. Rong, J. Zhang, D. Wang, Y. Li, Modulating the local coordination environment of single-atom catalysts for enhanced catalytic performance. Nano Res. **13**, 1842–1855 (2020). https://doi.org/10.1007/s12274-020-2755-3

27. Y. Zheng, Y. Jiao, Y. Zhu, Q. Cai, A. Vasileff et al., Molecule-level g-C_3N_4 coordinated transition metals as a new class of electrocatalysts for oxygen electrode reactions. J. Am. Chem. Soc. **139**, 3336–3339 (2017). https://doi.org/10.1021/jacs.6b13100

28. X. Wang, X. Chen, A. Thomas, X. Fu, M. Antonietti, Metal-containing carbon nitride compounds: a new functional organic–metal hybrid material. Adv. Mater. **21**, 1609–1612 (2009). https://doi.org/10.1002/adma.200802627

29. J. Gu, M. Jian, L. Huang, Z. Sun, A. Li et al., Synergizing metal–support interactions and spatial confinement boosts dynamics of atomic nickel for hydrogenations. Nat. Nanotechnol. **16**, 1141–1149 (2021). https://doi.org/10.1038/s41565-021-00951-y

30. S. Cao, H. Li, T. Tong, H.-C. Chen, A. Yu et al., Single-atom engineering of directional charge transfer channels and active sites for photocatalytic hydrogen evolution. Adv. Funct. Mater. **28**, 1802169 (2018). https://doi.org/10.1002/adfm.201802169

31. H. Zhang, C. Wang, H. Luo, J. Chen, M. Kuang et al., Iron nanoparticles protected by chainmail-structured graphene for durable electrocatalytic nitrate reduction to nitrogen. Angew. Chem. Int. Ed. **62**, e202217071 (2023). https://doi.org/10.1002/anie.202217071

32. X. Zou, X. Huang, A. Goswami, R. Silva, B.R. Sathe et al., Cobalt-embedded nitrogen-rich carbon nanotubes efficiently catalyze hydrogen evolution reaction at all ph values. Angew. Chem. Int. Ed. **53**, 4372–4376 (2014). https://doi.org/10.1002/anie.201311111

33. F. He, K. Li, C. Yin, Y. Wang, H. Tang et al., Single Pd atoms supported by graphitic carbon nitride, a potential oxygen reduction reaction catalyst from theoretical perspective. Carbon **114**, 619–627 (2017). https://doi.org/10.1016/j.carbon.2016.12.061

34. X. Chen, X. Zhao, Z. Kong, W.-J. Ong, N. Li, Unravelling the electrochemical mechanisms for nitrogen fixation on single transition metal atoms embedded in defective graphitic carbon nitride. J. Mater. Chem. A **6**, 21941–21948 (2018). https://doi.org/10.1039/C8TA06497K

35. Q. Wang, K. Liu, J. Fu, C. Cai, H. Li et al., Atomically dispersed s-block magnesium sites for electroreduction of CO_2 to CO. Angew. Chem. Int. Ed. **60**, 25241–25245 (2021). https://doi.org/10.1002/anie.202109329

36. Y. Jiao, Y. Zheng, P. Chen, M. Jaroniec, S.-Z. Qiao, Molecular scaffolding strategy with synergistic active centers to facilitate electrocatalytic co_2 reduction to hydrocarbon/alcohol. J. Am. Chem. Soc. **139**, 18093–18100 (2017). https://doi.org/10.1021/jacs.7b10817

37. G. Kresse, J. Furthmuller, Efficient iterative schemes for *ab initio* total-energy calculations using a plane-wave basis set. Phys. Rev. B **54**, 11169–11186 (1996). https://doi.org/10.1103/PhysRevB.54.11169

38. J.P. Perdew, K. Burke, M. Ernzerhof, Generalized gradient approximation made simple. Phys. Rev. Lett. **77**, 3865–3868 (1996). https://doi.org/10.1103/PhysRevLett.77.3865

39. B. Hammer, L.B. Hansen, J.K. Norskov, Improved adsorption energetics within density-functional theory using revised perdew-burke-ernzerhof functionals. Phys. Rev. B **59**, 7413 (1999). https://doi.org/10.1103/PhysRevB.59.7413

40. S. Grimme, Semiempirical GGA-type density functional constructed with a long-range dispersion correction. J. Comput. Chem. **27**, 1787–1799 (2006). https://doi.org/10.1002/jcc.20495

41. E. Skúlason, V. Tripkovic, M.E. Björketun, S. Gudmundsdóttir, G. Karlberg et al., Modeling the electrochemical hydrogen oxidation and evolution reactions on the basis of density functional theory calculations. J. Phys. Chem. C **114**, 18182–18197 (2010). https://doi.org/10.1021/jp1048887

42. G. Gao, A.P. O'Mullane, A. Du, 2D Mxenes: a new family of promising catalysts for the hydrogen evolution reaction. ACS Catal. **7**, 494–500 (2017). https://doi.org/10.1021/acscatal.6b02754

43. Z. Jin, P. Li, Y. Meng, Z. Fang, D. Xiao et al., Understanding the inter-site distance effect in single-atom catalysts for oxygen

electroreduction. Nat. Catal. **4**(7), 615–622 (2021). https://doi.org/10.1038/s41929-021-00650-w

44. T. Zhang, W. Li, K. Huang, H. Guo, Z. Li et al., Regulation of functional groups on graphene quantum dots directs selective CO_2 to CH_4 conversion. Nat. Commun. **12**, 5265 (2021). https://doi.org/10.1038/s41467-021-25640-1

45. R.M. Yadav, Z. Li, T. Zhang, O. Sahin, S. Roy et al., Amine-functionalized carbon nanodot electrocatalysts converting carbon dioxide to methane. Adv. Mater. **34**, 2105690 (2022). https://doi.org/10.1002/adma.202105690

46. Y. Xiao, G. Tian, W. Li, Y. Xie, B. Jiang et al., Molecule self-assembly synthesis of porous few-layer carbon nitride for highly efficient photoredox catalysis. J. Am. Chem. Soc. **141**, 2508–2515 (2019). https://doi.org/10.1021/jacs.8b12428

47. X. Zou, R. Silva, A. Goswami, T. Asefa, Cu-doped carbon nitride: Bio-inspired synthesis of H_2-evolving electrocatalysts using graphitic carbon nitride (g-C_3N_4) as a host material. Appl. Surf. Sci. **357**, 221–228 (2015). https://doi.org/10.1016/j.apsusc.2015.08.197

48. J. Ran, T.Y. Ma, G. Gao, X.-W. Du, S.Z. Qiao, Porous P-doped graphitic carbon nitride nanosheets for synergistically enhanced visible-light photocatalytic h_2 production. Energ. Environ. Sci. **8**, 3708–3717 (2015). https://doi.org/10.1039/C5EE02650D

49. Q. Han, B. Wang, J. Gao, Z. Cheng, Y. Zhao et al., Atomically thin mesoporous nanomesh of graphitic C_3N_4 for high-efficiency photocatalytic hydrogen evolution. ACS Nano **10**, 2745–2751 (2016). https://doi.org/10.1021/acsnano.5b07831

50. B. Yue, Q. Li, H. Iwai, T. Kako, J. Ye, Hydrogen production using zinc-doped carbon nitride catalyst irradiated with visible light. Sci. Technol. Adv. Mater. **12**, 034401 (2011). https://doi.org/10.1088/1468-6996/12/3/034401

51. Y. Zhou, F. Che, M. Liu, C. Zou, Z. Liang et al., Dopant-induced electron localization drives CO_2 reduction to C_2 hydrocarbons. Nat. Chem. **10**, 974–980 (2018). https://doi.org/10.1038/s41557-018-0092-x

52. H. Shang, X. Zhou, J. Dong, A. Li, X. Zhao et al., Engineering unsymmetrically coordinated Cu-S_1N_3 single atom sites with enhanced oxygen reduction activity. Nat. Commun. **11**, 3049 (2020). https://doi.org/10.1038/s41467-020-16848-8

53. X. Zhao, Y. Cao, L. Duan, R. Yang, Z. Jiang et al., Unleash electron transfer in C–H functionalization by mesoporous carbon-supported palladium interstitial catalysts. Natl. Sci. Rev. **8**, nwaa126 (2020). https://doi.org/10.1093/nsr/nwaa126

54. M. Li, N. Song, W. Luo, J. Chen, W. Jiang et al., Engineering surface oxophilicity of copper for electrochemical CO_2 reduction to ethanol. Adv. Sci. **10**, 2204579 (2022). https://doi.org/10.1002/advs.202204579

55. J. Xu, X. Zheng, Z. Feng, Z. Lu, Z. Zhang et al., Organic wastewater treatment by a single-atom catalyst and electrolytically produced H_2O_2. Nat. Sustain. **4**, 233–241 (2021). https://doi.org/10.1038/s41893-020-00635-w

56. J. Liang, Y. Zheng, J. Chen, J. Liu, D. Hulicova-Jurcakova et al., Facile oxygen reduction on a three-dimensionally ordered macroporous graphitic C_3N_4/carbon composite electrocatalyst. Angew. Chem. Int. Ed. **51**, 3892–3896 (2012). https://doi.org/10.1002/anie.201107981

57. G. Zhu, R. Guo, W. Luo, H.K. Liu, W. Jiang et al., Boron doping-induced interconnected assembly approach for mesoporous silicon oxycarbide architecture. Natl. Sci. Rev. **8**, nwaa152 (2020). https://doi.org/10.1093/nsr/nwaa152

58. Y. Zhang, L.-Z. Dong, S. Li, X. Huang, J.-N. Chang et al., Coordination environment dependent selectivity of single-site-Cu enriched crystalline porous catalysts in CO_2 reduction to CH_4. Nat. Commun. **12**, 6390 (2021). https://doi.org/10.1038/s41467-021-26724-8

59. J. Feng, L. Zheng, C. Jiang, Z. Chen, L. Liu et al., Constructing single Cu-N_3 sites for CO_2 electrochemical reduction over a wide potential range. Green Chem. **23**, 5461–5466 (2021). https://doi.org/10.1039/D1GC01914G

60. J.-D. Yi, R. Xie, Z.-L. Xie, G.-L. Chai, T.-F. Liu et al., Highly selective CO_2 electroreduction to CH_4 by in situ generated Cu_2O single-type sites on a conductive mof: stabilizing key intermediates with hydrogen bonding. Angew. Chem. Int. Ed. **59**, 23641–23648 (2020). https://doi.org/10.1002/anie.202010601

61. Y. Pan, H. Li, J. Xiong, Y. Yu, H. Du et al., Protecting the state of cu clusters and nanoconfinement engineering over hollow mesoporous carbon spheres for electrocatalytical C-C coupling. Appl. Catal. B: Environ. **306**, 121111 (2022). https://doi.org/10.1016/j.apcatb.2022.121111

62. Y.-Y. Liu, H.-L. Zhu, Z.-H. Zhao, N.-Y. Huang, P.-Q. Liao et al., Insight into the effect of the d-orbital energy of copper ions in metal–organic frameworks on the selectivity of electroreduction of CO_2 to CH_4. ACS Catal. **12**(5), 2749–2755 (2022). https://doi.org/10.1021/acscatal.1c04805

63. Y. Cao, S. Chen, Q. Luo, H. Yan, Y. Lin et al., Atomic-level insight into optimizing the hydrogen evolution pathway over a Co_1-N_4 single-site photocatalyst. Angew. Chem. Int. Ed. **129**(40), 12359–12364 (2017). https://doi.org/10.1002/ange.201706467